


Vibration response of monolayer 1H-MoTe₂ to equibiaxial strain

Wei Yang ¹, Ling-Yu Zhu,¹ Tian Zhou,¹ Tao-Jun Yang,¹ Yi-Bo Yan,¹ Jia-Jun Li,¹ Fa-Wei Zheng,² Yu Yang,² Xiao-Hui Wang,^{1,*} Wen-Bo Xu,^{3,†} and Ping Zhang^{2,4,‡}

¹Beijing Key Laboratory of Work Safety Intelligent Monitoring, Beijing University of Posts and Telecommunications, Beijing 100876, People's Republic of China

²Institute of Applied Physics and Computational Mathematics, Beijing 100088, People's Republic of China

³Key Lab of Universal Wireless Communications, Ministry of Education, Beijing University of Posts and Telecommunications, Beijing 100876, People's Republic of China

⁴Beijing Computational Science Research Center, Beijing 100084, People's Republic of China



(Received 9 July 2020; revised 18 October 2020; accepted 26 October 2020; published 25 November 2020)

Based on density functional theory and density functional perturbation theory calculations, we systematically investigate the vibration responses of monolayer 1H-MoTe₂ to equibiaxial strains. It is found that, at the Γ point, the frequency shift of Raman-active modes (E' , A'_1 , and E'') and infrared-active modes (A'_2 and E') show domelike shapes; that is, their frequencies decrease monotonically under tensile strains but first increase and then decrease rapidly under compressive strains. The frequency-shift behaviors are revealed to come from vibration responses to both bond stretching and bond-angle bending in strained 1H-MoTe₂. At the K point, a special acoustic mode becomes soft because its frequency drops to zero at a compressive strain of -11.27% . We find that electron occupancies in Mo d_{z^2} , Te p_x , and Te p_y orbitals weaken the vibration mode at K , which exhibits the in-plane vibration of Mo atoms and out-of-plane vibration of Te atoms. On the other hand, compressive strains enhance the Fermi surface nesting and abruptly soften the vibration frequency for one acoustic mode at K . Our results point out a way to detect the strain status of monolayer 1H-MoTe₂ by measuring the vibration frequencies.

DOI: [10.1103/PhysRevB.102.195431](https://doi.org/10.1103/PhysRevB.102.195431)

I. INTRODUCTION

The transition metal dichalcogenide (TMD) monolayer, a widely studied two-dimensional material family [1,2], contains several polymorphs, such as the trigonal prismatic 1H phase, octahedral 1T phase, and distorted orthorhombic 1T' phase [3,4]. For most TMDs monolayers, except 1T'-WTe₂, the lowest-energy phase is the semiconducting 1H structure. Recently, the MoTe₂ monolayer has attracted remarkable attention in optoelectronic devices and field effect transistors because of its promising electronic, optical, and phase-transition properties [5–9]. Several experimental and theoretical works have explored different means to attain phase transition of 1H-MoTe₂, such as chemical modifications [10–14], gating or electrostatic doping [11,15–18], and uniaxial strain [4,19,20]. For instance, Song *et al.* [19] reported a phase transition of MoTe₂ from 1H to 1T' under small uniaxial strain of 0.2% using an atomic force microscope tip. But along the equibiaxial direction, 1H-MoTe₂ can withstand a larger strain (tensile strain below 10% and entire compressive strain) without a phase transition [4,21]. Biaxial

strain provides a wide range for tuning and controlling the mechanical [22–24], electronic [25–27], thermal transport [28], work function [29], and magnetic [30,31] performance of 1H-MoTe₂. However, the crystal vibration (phonon) properties and, in particular, frequency-shift behaviors of phonon modes for monolayer 1H-MoTe₂ remain unclarified in the case of equibiaxial deformation, especially for compressive strains.

Lattice vibration is the most direct response to geometry deformation of atomic structures under external strains [32,33]. On the other hand, the frequency shift of phonon modes can be used to trace and monitor the strain status. For example, the frequency of Raman- or infrared-active modes can be detected by the Raman or infrared spectrum so that the strain can be quantified [34,35]. Moreover, a downshift of phonon frequency into zero is always called phonon softening and corresponds to the structural transition or mechanical failure of a material [36]. In general, a tensile strain can lead to the softening of phonon modes [37,38], which results in thermal conductivity reduction [28] or electron-phonon coupling enhancement [39]. However, for monolayer 1H-MoTe₂, we find that a soft mode occurs under compressive strain, but a blueshift in frequency of this mode occurs under tensile strains. Furthermore, the frequency of Raman- and infrared-active modes exhibits a domelike shape under equibiaxial strains, and the maximum value emerges at compressive strains. We also try to explain these anomalous and interesting phenomena in terms of atomic bond configurations and electronic structure characteristics of 1H-MoTe₂ under equibiaxial strains. Our findings provide a reference database

*Author to whom correspondence should be addressed: wangxiaohui@bupt.edu.cn

†Author to whom correspondence should be addressed: xuwb@bupt.edu.cn

‡Author to whom correspondence should be addressed: zhang_ping@iapcm.ac.cn

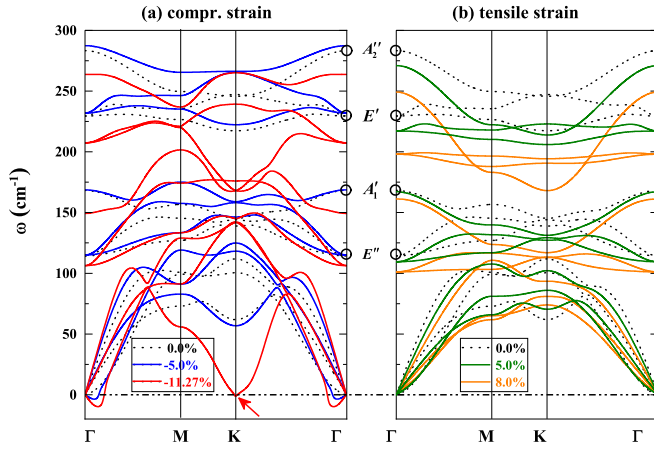


FIG. 1. Phonon dispersion curves for monolayer $1H$ -MoTe $_2$ at four representative equibiaxial strains. (a) Compressive strains of -5% (blue lines) and -11.27% (red lines). (b) Tensile strains of 5% (green lines) and 8% (orange lines). The black dotted curves correspond to intrinsic (0%) phonon spectra for comparison with the strained one. The red arrow is used to identify the K soft mode. The black circles mark optical modes at the Γ point. The q point labels Γ , M , and K correspond to $(0, 0)$, $(1/2, 0)$, and $(1/3, 1/3)$, respectively, in the fraction of the reciprocal lattice vectors.

for the vibration behaviors of strained $1H$ -TMD monolayers and develop a mechanism to directionally control strain for the rational design of TMDs-based flexible devices.

II. COMPUTATIONAL METHOD

To thoroughly explore the vibration properties of strained $1H$ -MoTe $_2$, we first calculate their phonon dispersion curves, which is carried out within plane-wave pseudopotential method as implemented in the QUANTUM ESPRESSO package [4,40]. We use the Perdew-Burke-Ernzerhof [41] functional with a plane-wave cutoff energy of 40 Ry and a charge density cutoff energy of 400 Ry to get a total energy accuracy better than 10^{-8} Ry. A $32 \times 32 \times 1$ k -point mesh is used for Brillouin zone integration over electronic states, and an $8 \times 8 \times 1$ q -point grid is used to obtain dynamic matrices for the phonon calculations. Figure 1 shows the calculated phonon spectra of $1H$ -MoTe $_2$ under different equibiaxial strains, $\varepsilon = \frac{a}{a_0} - 1$, where a and a_0 are the strained and equilibrium lattice constants of $1H$ -MoTe $_2$, respectively. It should be noted that, in Fig. 1(a), there are imaginary frequencies of the acoustic phonon branch near the Γ point, but this kind of imaginary frequency is irrelevant to the main discussion

TABLE I. The phonon frequencies (in cm^{-1}) of optical modes at the Γ point for $1H$ -MoTe $_2$ from Raman experiments and first-principles calculations.

Symmetry	Experiment						Theory				
	Ref. [42]	Ref. [43]	Ref. [44]	Ref. [45]	Ref. [46]	Ref. [47]	Ref. [48]	Ref. [49]	Ref. [50]	Ref. [28]	Our work
A_2''								285	285.21	286.02	285.30
E'	234	236.5	234	234.6	235	236	236.9	230	230.16	231.09	230.46
A_1'	170	171.5	170	168.4	174	171	172.2	167	170.03	170.25	170.28
E''							116.9	114	114.54	114.78	114.33

in our work. A freestanding two-dimensional (2D) material under compressive strain has a more stable buckling state than a perfect plane. Thus, negative frequency exists around the Γ point in the phonon dispersions of the perfect plane. It can be suppressed by many methods in experiment; for instance, by putting a 2D layer on a substrate, the interaction between the film and substrate may stabilize the film. In Fig. 1, we also reproduce the phonons for unstrained $1H$ -MoTe $_2$, and the frequencies of six optical modes at the Γ wave vector, marked by black circles, are 285.30 cm^{-1} , 230.46 cm^{-1} (doubly degenerate), 170.28 cm^{-1} , and 114.33 cm^{-1} (doubly degenerate), which are quite consistent with theoretical and experimental results [28,42–50], as shown in Table I.

III. RESULTS AND DISCUSSION

We find that frequencies for optical phonon branches are normally upshifted under compressive strains and downshifted under tensile strains for moderate strains between -5% and 5% , as shown in Fig. 1. However, for acoustic phonon branches, there is an anomalous mode at the K wave vector (named the K mode), for its frequency downshifted under compressive strain but upshifted under tensile strain. Especially, when the applied compressive strain reaches a critical value of -11.27% , the frequency of this mode drops to zero, which can be named the K soft mode [see the red arrow in Fig. 1(a)]. It is also anomalous that, under larger compressive strain, the frequencies of the optical phonon branches no longer shift upward, but downward, which can be clearly seen from the red curves in Fig. 1(a). Under larger tensile strain (we select 8% as the maximum value to ensure MoTe $_2$ remains in the $1H$ phase), the frequencies of optical branches continue to downshift, and that of the K mode continues to upshift, as the orange curves show in Fig. 1(b). Next, we will systematically explore these frequency-shift behaviors of phonon modes in monolayer $1H$ -MoTe $_2$ under equibiaxial strains.

At the Γ point, the optical phonon modes are characterized by the relative vibration of different kinds of atoms, inducing electric dipole moments, which allow them to interact with the electromagnetic waves, such as Raman scattering and infrared absorption. Therefore, we will focus on the Raman- and infrared-active modes in the optical phonon branches for strained $1H$ -MoTe $_2$. Based on factor group analysis, monolayer $1H$ -MoTe $_2$ belongs to the D_{3h}^1 point group, and the irreducible representations can be expressed as $\Gamma_{\text{optical}} = A_1' + A_2'' + 2E' + 2E''$, where A is a single mode with one-dimensional representation and E is a doubly degenerate mode with two-dimensional representation; the superscript prime and double prime represent the mode is symmetric and

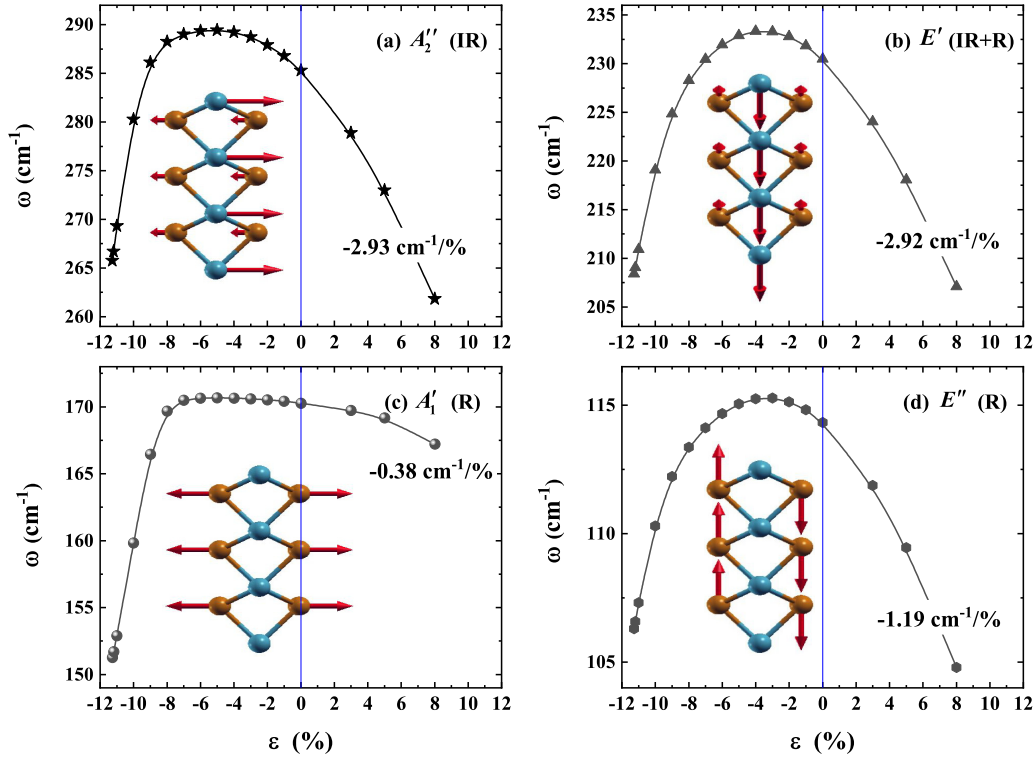


FIG. 2. The calculated frequencies of (a) A_2'' (IR), (b) E' [IR+Raman (R)], (c) A_1' (R), and (d) E'' (R) modes versus equibiaxial strains. The corresponding atomic vibration figures are in the insets, where cyan and orange balls represent Mo and Te atoms, respectively. The crystal structure is a side view of monolayer $1H$ -MoTe₂ in the yz plane.

antisymmetric to a mirror plane m , and subscripts 1 and 2 represent the mode is symmetric and antisymmetric to the rotation axis C_n . According to our calculated eigenvectors of the optical modes for $1H$ -MoTe₂, their atomic vibration displacements are plotted in the inset in Fig. 2 in order of frequency from high to low, so the corresponding irreducible representations should be A_2'' , E' , A_1' , and E'' , respectively, based on careful analysis of vibration symmetries. Furthermore, according to selection rules in the character table of D_{3h} , A_2'' is an infrared-active mode, E' is both a Raman- and infrared-active mode, A_1' and E'' are Raman-active modes.

Now we can select the frequency values of each mode under different strains based on the symmetry characteristics discussed above since the D_{3h} symmetry is maintained for $1H$ -MoTe₂ under equibiaxial strains between -11.3% and 8% in our study. The frequency-strain curves of A_2'' , E' , A_1' , and E'' are plotted in Figs. 2(a), 2(b), 2(c), and 2(d), respectively. Under biaxial tensile strains, the frequency of each mode decreases monotonically. The slope for a frequency change of A_2'' and E' (double atomic vibration modes) is larger than that of A_1' and E'' (single atomic vibration modes), which may be due to the different effective mass, resulting in different responses of the vibration frequency to the applied strain. Under biaxial compressive strains, the frequency value initially increases, then passes through a maximum at a critical strain of -6% for A_2'' and A_1' and -4% for E'' and E' , and then decreases rapidly. On the one hand, the influence of biaxial strain on in-plane E modes is greater than that of out-of-plane A modes, so the frequency transition of E modes is earlier than that of

A modes. On the other hand, the anomalous redshift under higher compressive strains might result from the complex interplay between bond stretching and bond-angle bending in the $1H$ -MoTe₂ lattice. For this reason, we draw the atomic bond configurations of monolayer $1H$ -MoTe₂ under biaxial strain, as shown in Fig. 3. After complete atomic relaxation, the bond angles of Mo-Te-Mo and Te-Mo-Te show almost linear change with external strains, but the bond length of Mo-Te and the vertical distance of Te-Te show nonlinear change with compressive strains; especially, $d_{\text{Mo-Te}}$ even increases under higher compressive strain, as shown by the black line with stars in Fig. 3(a). Therefore, the frequencies are redshifted under higher compressive strains. We hope this can be tested by future Raman or infrared experiments of strained $1H$ -MoTe₂.

For the acoustic phonon branches of monolayer $1H$ -MoTe₂, there is a special mode at the K point, as shown in Fig. 1(a). Next, we will explore the K mode and analyze why the K mode softens under compressive strains. Along the high-symmetry axis M - K - Γ , we cut out the dispersion curve containing the K mode with different external strains, as shown in the inset of Fig. 4(a). Then we select the frequency of the K mode and plot it as a function of equibiaxial strain in Fig. 1(a), from which one can see that the frequency decreases monotonically with strain from 8% to -7% , then drops abruptly, and at last turns to zero at a compressive strain of -11.27% , resulting in a soft mode. A phonon mode that goes soft will grow in amplitude until the structure is driven to another stable state. The incremental atomic displacements can be derived by multiplying $e^{i\frac{2n\pi}{3}}$ (n is an integer) by eigenvectors of three atoms in a primitive cell. According to the

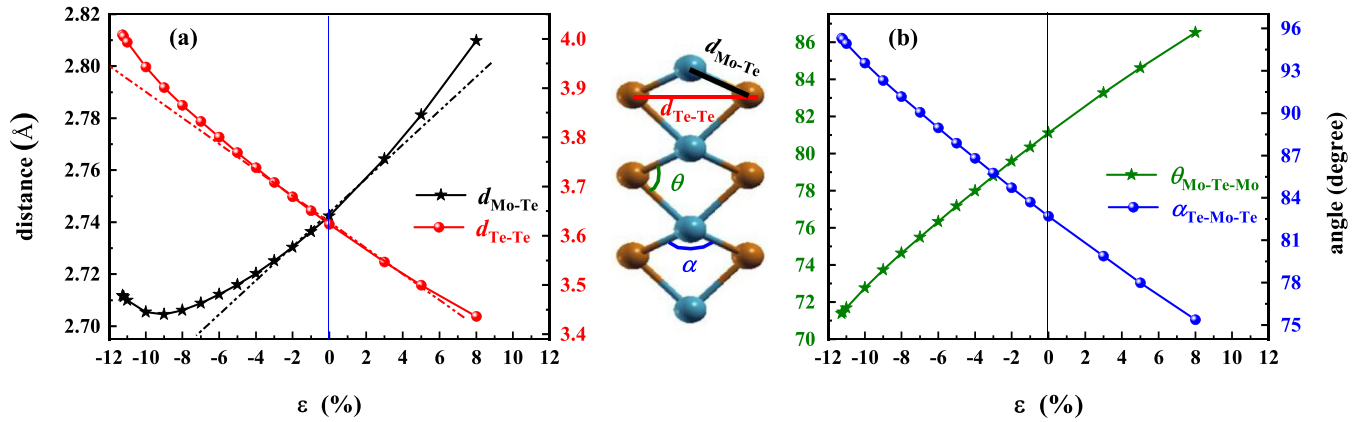


FIG. 3. The calculated (a) Mo-Te bond length (black stars) and vertical distance of Te-Te along the z direction (red balls) and (b) Mo-Te-Mo bond angle θ (green stars) and Te-Mo-Te bond angle α (blue balls) as functions of equibiaxial strain. The inset crystal configurations of monolayer 1H-MoTe₂ in the yz plane are used to depict these calculated variables.

vibration characteristic of the phonon mode at the K point shown in Fig. 4(b), the unit cell of the K mode should be a nine-atom cell (blue parallelogram), which is 3 times the size of the primitive cell (red parallelogram). Figures 4(c1) and 4(c2) show the top view and side view of atomic vibration displacements within the K cell, respectively. One can see that Mo atoms vibrate in the plane of monolayer 1H-MoTe₂, while Te atoms vibrate out of the plane. Moreover, the Mo atoms of the K mode vibrate in different directions, forming a congruent triangle, which will result in a nonuniform distribution. Distorting along the K mode, the monolayer 1H-MoTe₂ will become unstable and undergo a phase transition. Our calculations show that, under compressive strain, Mo atoms tend to redistribute in a nonuniform pattern and result in the K mode softening.

The electronic reason for the vibration responses of the K mode to compressive strain is then analyzed through the band structure and Fermi surface (FS) calculations. Figures 5(a) and 5(b) show our obtained orbital-resolved density of states (DOS) and band structure of monolayer 1H-MoTe₂ at -11.27% , respectively. The corresponding FS is shown in Fig. 5(c). One can see that, at a compressive strain of -11.27% , monolayer 1H-MoTe₂ is metallic, which is consistent with Kumar's work indicating that semiconducting 1H-MoTe₂ becomes metallic at a compressive strain of -11% [27]. Moreover, the electrons around E_F mainly occupy Mo d_z , Te p_x , and Te p_y orbitals, i.e., the out-of-plane orbitals of Mo states and in-plane orbitals of Te states. Therefore, the in-plane vibration of Mo atoms and out-of-plane vibration of Te atoms would be weaker, further explaining the reason for

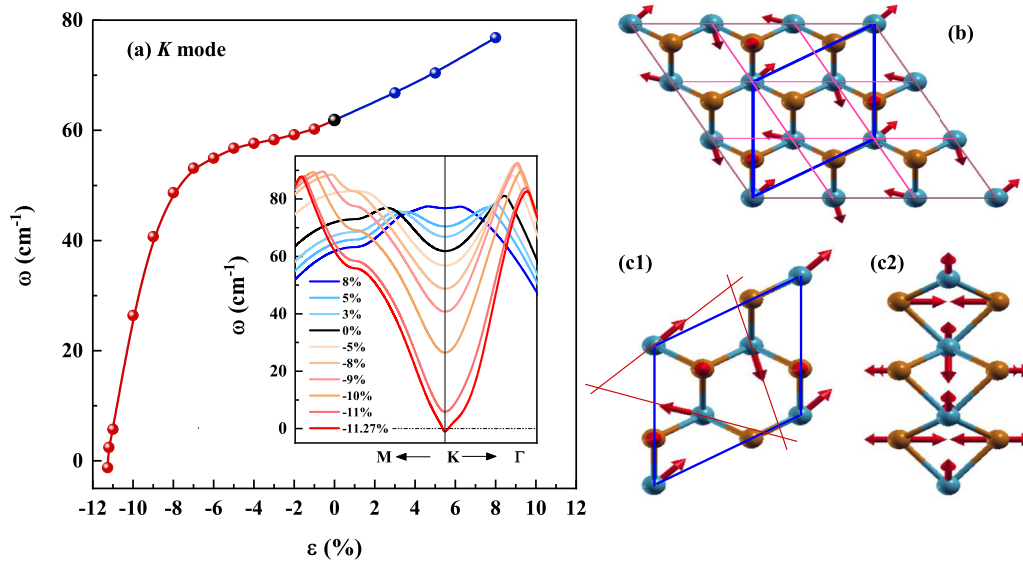


FIG. 4. (a) The calculated frequencies of the K mode as a function of equibiaxial strains for monolayer 1H-MoTe₂. The inset of (a) is the dispersion curve for the acoustic branch containing the K mode along the high-symmetry axis $M-K-\Gamma$. Blue and red lines represent the results of tensile and compressive strains, respectively, and the line brightness changes from light to dark with increasing strain. (b) The atomic vibration displacements of the K mode. The unit cell of the K mode is denoted by a blue parallelogram, and the primitive cell is denoted by a red parallelogram. The atomic vibration displacements in (c1) the top view and (c2) side view.

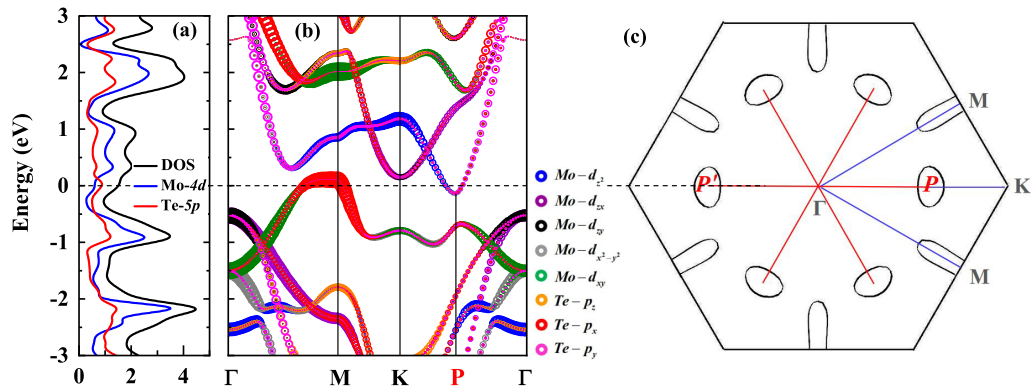


FIG. 5. The calculated electronic structures of monolayer $1H$ - MoTe_2 under equibiaxial compressive strain of -11.27% . (a) DOS and orbital-resolved local DOSs. (b) Orbital-resolved band structure displayed with circles whose sizes are proportional to the weight of each orbital. (c) The corresponding Fermi surface. Note that, in (b) and (c), the special wave vector $P = (\frac{9}{50}, \frac{9}{50})$ in fractions of the reciprocal lattice vectors.

the K mode softening. However, the underlying reason for the K mode softening at the K point rather than other wave vectors is not fully understood. We think that this is associated with the strain enhancement of the FS nesting in $1H$ - MoTe_2 . As shown in Fig. 5(c), along the Γ - K line, there are two electron pockets labeled by P' and P , where $P = (\frac{9}{50}, \frac{9}{50})$. The nesting vector of the two electron pockets $P - P' = (\frac{9}{25}, \frac{9}{25})$ is quite close to the vector of the K mode $K = (\frac{1}{3}, \frac{1}{3})$. It arises from the screening effects of electrons on the atomic vibrations [51], which change the vibrations abruptly at the special K point. Therefore, the phonon mode of monolayer $1H$ - MoTe_2 softens at the K point under equibiaxial compressive strain.

IV. CONCLUSIONS

In conclusion, by using density functional theory and density functional perturbation theory simulations, we have systematically explored the phonon spectra of monolayer $1H$ - MoTe_2 under equibiaxial strains. Our results demonstrate that,

for optical modes at the Γ point, their frequency exhibits a domelike shift with external strains, but for an acoustic mode at the K point, the frequency decreases monotonically and eventually drops to zero under compressive strain. These are associated with the response of vibration characteristics to the variations of atomic bond configurations (length, angles, and strength) caused by applied strains. The K soft mode resulting from the FS nesting can characterize structural instability, determine thermal properties, and enhance electron-phonon coupling of strained $1H$ - MoTe_2 . Our results make strained $1H$ - MoTe_2 attractive for application in flexible electronic, thermoelectric, and superconducting devices in which the strain intensity can be quantified by Raman or infrared spectra.

ACKNOWLEDGMENTS

This work was supported by the National Natural Science Foundation of China under Grants No. 11625415 and No. 61605014 and the Science Challenge Project under Grant No. TZ2016001.

- [1] J. A. Wilson and A. D. Yoffe, *Adv. Phys.* **18**, 193 (1969).
- [2] J. D. Zhou, J. H. Lin, X. W. Huang, Y. Zhou, Y. Chen, J. Xia, H. Wang, Y. Xie, H. M. Yu, J. C. Lei, D. Wu, F. C. Liu, Q. D. Fu, Q. S. Zeng, C. H. Hsu, C. L. Yang, L. Lu, T. Yu, Z. X. Shen, H. Lin *et al.*, *Nature (London)* **556**, 355 (2018).
- [3] X. F. Qian, J. W. Liu, L. Fu, and J. Li, *Science* **346**, 1344 (2014).
- [4] K. A. N. Duerloo, Y. Li, and E. J. Reed, *Nat. Commun.* **5**, 4214 (2014).
- [5] W. H. Hou, A. Azizimanesh, A. Sewaket, T. Pena, C. Watson, M. Liu, H. Askari, and S. M. Wu, *Nat. Nanotechnol.* **14**, 668 (2019).
- [6] J. W. You, Y. Ye, K. Cai, D. M. Zhou, H. M. Zhu, R. Y. Wang, Q. F. Zhang, H. W. Liu, Y. T. Cai, D. Lu, J.-K. Kim, L. Gan, T. Y. Zhai, and Z. T. Luo, *Nano Res.* **13**, 1636 (2020).
- [7] J. Chen, Y. Shan, Q. Wang, J. Zhu, and R. Liu, *Nanotechnology* **31**, 295201 (2020).
- [8] L. Meckbach, J. Hader, U. Huttner, J. Neuhaus, J. T. Steiner, T. Stroucken, J. V. Moloney, and S. W. Koch, *Phys. Rev. B* **101**, 075401 (2020).
- [9] Y. Z. Li, J. X. Zhang, D. D. Huang, H. Sun, F. Fan, J. B. Feng, Z. Wang, and C. Z. Ning, *Nat. Nanotechnol.* **12**, 987 (2017).
- [10] S. Cho, S. Kim, J. H. Kim, J. Zhao, J. Seok, D. H. Keum, J. Baik, D.-H. Choe, K. J. Chang, K. Suenaga, S. W. Kim, Y. H. Lee, and H. Yang, *Science* **349**, 625 (2015).
- [11] C. X. Zhang, K. C. Santosh, Y. F. Nie, C. P. Liang, W. G. Vandenberghe, R. C. Longo, Y. P. Zheng, F. T. Kong, S. Hong, R. M. Wallace, and K. Cho, *ACS Nano* **10**, 7370 (2016).
- [12] D. Rhodes, D. A. Chenet, D. A. Janicek, B. E. Nyby, C. Lin, Y. Jin, W. Edelberg, D. Mannebach, E. Finney, N. Antony, A. Schiros, T. Klarr, T. Mazzoni, A. Chin, M. Chiu, Y. Zheng, W. Zhang, Q. R. Ernst, F. Dadayp, J. I. Tong *et al.*, *Nano Lett.* **17**, 1616 (2017).

- [13] H. Nan, J. Jiang, S. Xiao, Z. Chen, Z. Luo, L. Zhang, X. Zhang, H. Qi, X. Gu, X. Wang, and Z. Ni, *Nat. Nanotechnol.* **30**, 034004 (2019).
- [14] P. Manchanda, P. Kumar, and P. Dev, *Phys. Rev. B* **101**, 144104 (2020).
- [15] Y. Li, K. A. N. Duerloo, K. Wauson, and E. J. Reed, *Nat. Commun.* **7**, 10671 (2016).
- [16] Y. Wang, J. Xiao, H. Zhu, Y. Li, Y. Alsaïd, K. Y. Fong, Y. Zhou, S. Wang, S. Wu, Y. Wang, A. Zettl, E. J. Reed, and X. Zhang, *Nature (London)* **550**, 487 (2017).
- [17] A. Krishnamoorthy, L. Bassman, R. K. Kalia, A. Nakano, F. Shimojo, and P. Vashishta, *Nanoscale* **10**, 2742 (2018).
- [18] F. Zhang, H. Zhang, S. Krylyuk, C. A. Milligan, Y. Zhu, D. Y. Zemlyanov, L. A. Bendersky, B. P. Burton, A. V. Davydov, and J. Appenzeller, *Nat. Mater.* **18**, 55 (2019).
- [19] S. Song, D. H. Keum, S. Cho, D. Perello, Y. Kim, and Y. H. Lee, *Nano Lett.* **16**, 188 (2016).
- [20] J. Berry, S. Zhou, J. Han, D. J. Srolovitz, and M. P. Haataja, *Nano Lett.* **17**, 2473 (2017).
- [21] H. H. Huang, X. Fan, D. J. Singh, H. Chen, Q. Jiang, and W. T. Zheng, *Phys. Chem. Chem. Phys.* **18**, 4086 (2016).
- [22] B. Mortazavi, G. R. Berdiyrov, M. Makaremi, and T. Rabczuk, *Extreme Mech. Lett.* **20**, 65 (2018).
- [23] Y. Sun, J. Pan, Z. Zhang, K. Zhang, J. Liang, W. Wang, Z. Yuan, Y. Hao, B. Wang, J. Wang, Y. Wu, J. Zheng, L. Jiao, S. Zhou, K. Liu, C. Cheng, W. Duan, Y. Xu, Q. Yan, and K. Liu, *Nano Lett.* **19**, 761 (2019).
- [24] J. Li, N. V. Medhekar, and V. B. Shenoy, *J. Phys. Chem. C* **117**, 15842 (2013).
- [25] I. Ahmad, S. A. Khan, M. Idrees, M. Haneef, I. Shahid, H. U. Din, S. A. Khan, and B. Amin, *Phys. B (Amsterdam, Neth.)* **545**, 113 (2018).
- [26] W. S. Yun, S. W. Han, S. C. Hong, I. G. Kim, and J. D. Lee, *Phys. Rev. B* **85**, 033305 (2012).
- [27] A. Kumar and P. K. Ahluwalia, *Phys. B (Amsterdam, Neth.)* **419**, 66 (2013).
- [28] A. Shafique and Y. H. Shin, *Phys. Chem. Chem. Phys.* **19**, 32072 (2017).
- [29] N. A. Lanzillo, A. J. Simbeck, and S. K. Nayak, *J. Phys.: Condens. Matter* **27**, 175501 (2015).
- [30] Y. W. Zhao, Y. Li, M. X. Liu, K. W. Xu, and F. Ma, *J. Phys. Chem. C* **124**, 4299 (2020).
- [31] J. Liu, Y. Q. Ma, M. Y. Zhao, Y. Li, X. Q. Dai, and Y. N. Tang, *J. Mater. Sci.* **53**, 5114 (2018).
- [32] S. K. Deng, A. V. Sumant, and V. Berry, *Nano Today* **22**, 14 (2018).
- [33] Z. H. Dai, L. Q. Liu, and Z. Zhang, *Adv. Mater.* **31**, 1805417 (2019).
- [34] W. Yang, Y. Yang, F. W. Zheng, and P. Zhang, *J. Chem. Phys.* **139**, 214708 (2013).
- [35] W. Yang, Z.-Y. Yuan, Y.-Q. Luo, Y. Yang, F.-W. Zheng, Z.-H. Hu, X.-H. Wang, Y.-A. Liu, and P. Zhang, *Phys. Rev. B* **99**, 235401 (2019).
- [36] J. D. Axe and G. Shirane, *Phys. Today* **26**(9), 32 (1973).
- [37] C. A. Marianetti and H. G. Yevick, *Phys. Rev. Lett.* **105**, 245502 (2010).
- [38] W. Yang, Y. Yang, F. W. Zheng, and P. Zhang, *Appl. Phys. Lett.* **103**, 183106 (2013).
- [39] C. Si, Z. Liu, W. Duan, and F. Liu, *Phys. Rev. Lett.* **111**, 196802 (2013).
- [40] P. Giannozzi, S. Baroni, N. Bonini, M. Calandra, R. Car, C. Cavazzoni, D. Ceresoli, G. L. Chiarotti, M. Cococcioni, I. Dabo, A. Dal Corso, S. de Gironcoli, S. Fabris, G. Fratesi, R. Gebauer, U. Gerstmann, C. Gougoussis, A. Kokalj, M. Lazzeri, L. Martin-Samos *et al.*, *J. Phys.: Condens. Matter* **21**, 395502 (2009).
- [41] J. P. Perdew, K. Burke, and M. Ernzerhof, *Phys. Rev. Lett.* **77**, 3865 (1996).
- [42] M. Yamamoto, S. T. Wang, M. Ni, Y. F. Lin, S. L. Li, S. Aikawa, W. B. Jian, K. Ueno, K. Wakabayashi, and K. Tsukagoshi, *ACS Nano* **8**, 3895 (2014).
- [43] G. Froehlicher, E. Lorchat, F. Fernique, C. Joshi, A. Molina-Sanchez, L. Wirtz, and S. Berciaud, *Nano Lett.* **15**, 6481 (2015).
- [44] C. Ruppert, O. B. Aslan, and T. F. Heinz, *Nano Lett.* **14**, 6231 (2014).
- [45] C. Kim, S. Issarapanacheewin, I. Moon, K. Y. Lee, C. Ra, S. Lee, Z. Yang, and W. J. Yoo, *Adv. Electron. Mater.* **6**, 1900964 (2020).
- [46] Y. F. Lin, Y. Xu, S. T. Wang, S. L. Li, M. Yamamoto, A. Aparecido Ferreira, W. W. Li, H. B. Sun, S. Nakaharai, W. B. Jian, K. Ueno, and K. Tsukagoshi, *Adv. Mater.* **26**, 3263 (2014).
- [47] D. Zakhidov, D. A. Rehn, E. J. Reed, and A. Salleo, *ACS Nano* **14**, 2894 (2020).
- [48] H. Guo, T. Yang, M. Yamamoto, L. Zhou, R. Ishikawa, K. Ueno, K. Tsukagoshi, Z. Zhang, M. S. Dresselhaus, and R. Saito, *Phys. Rev. B* **91**, 205415 (2015).
- [49] Y. Ding, Y. Wang, J. Ni, L. Shi, S. Shi, and W. Tang, *Phys. B (Amsterdam, Neth.)* **406**, 2254 (2011).
- [50] M. Kan, H. G. Nam, Y. H. Lee, and Q. Sun, *Phys. Chem. Chem. Phys.* **17**, 14866 (2015).
- [51] W. Kohn, *Phys. Rev. Lett.* **2**, 393 (1959).